

**Supplementary Information for:**  
**Tailoring the thermal expansion of graphene via controlled defect  
creation**

Guillermo López-Polín,<sup>1</sup> Maria Ortega,<sup>2</sup> J. G. Vilhena,<sup>2,3</sup> Irene Alda,<sup>1</sup> J.  
Gomez-Herrero,<sup>1,4</sup> Pedro A. Serena,<sup>3</sup> C. Gomez-Navarro,<sup>1,4</sup> and Rubén Pérez<sup>2,4</sup>

<sup>1</sup>*Departamento de Física de la Materia Condensada,  
Universidad Autónoma de Madrid, E-28049 Madrid, Spain*

<sup>2</sup>*Departamento de Física Teórica de la Materia Condensada,  
Universidad Autónoma de Madrid, E-28049 Madrid, Spain*

<sup>3</sup>*Instituto de Ciencia de Materiales de Madrid (ICMM), CSIC,  
c/ Sor Juana Ines de la Cruz 3, E-28049 Madrid, Spain*

<sup>4</sup>*Condensed Matter Physics Center (IFIMAC),  
Universidad Autónoma de Madrid, E-28049 Madrid, Spain*

## Part I: EXPERIMENTS

### SI1. SAMPLE PREPARATION AND DESCRIPTION.

Substrates with circular wells were obtained in Si/SiO<sub>2</sub> patterned with optical lithography and reactive ion etching. Graphene monolayers obtained by mechanical exfoliation of natural graphite were first identified on these substrates by optical microscopy and then corroborated by Raman spectroscopy as described in in ref. 1. AFM images in non contact mode showed that each graphene flake usually covers several of these circular well forming graphene drumhead structures. As reported previously<sup>2</sup>, we observed that graphene flakes adheres to the wall of the wells for 2–6 nm. Only monolayered membranes showing a flat and featureless surface (i.e. absence of bubbles or wrinkles) were selected for this study.

### SI2. INDENTATION CURVES.

AFM images and indentation curves were measured with a Nanotec commercial microscope and WSxM software package<sup>3</sup>. These curves were acquired at the center of the suspended area with standard silicon probes with nominal force constant of 3 N/m and tip radius  $R_{TIP} = 30\text{nm}$  from Nanosensors. This ensures that the ratio between the radius of the graphene drum and the tip  $R_{DRUM}/R_{TIP} > 10$ , allowing the use of equation 1 in the main text (see ref. 4 for a detailed explanation). Each cantilever was calibrated during experiments using Sader method<sup>5</sup>, leading to values between 1.5-2.8 N/m. While we have not observe any variation at indentations speeds between 10-1000 nm/s all the indentation curves for this study were acquired at a fixed rate of 90 nm/s.

In order to use equation 1 in the main text, indentation has to be accurately estimated. Indentation ( $\delta$ ) is not a direct experimental measure; it is calculated from the differences of the relative displacement of the sample and the tip on the non-deforming SiO<sub>2</sub> substrate. In order to correctly determine  $\delta$  we always perform a calibration indentation curve on the nearby substrate before and after acquiring curves on the membrane. Representative curves are illustrated in figure S1.

Since measurements were acquired at varying temperature we also checked that the sample displacement calibration did not change upon this temperature changes.

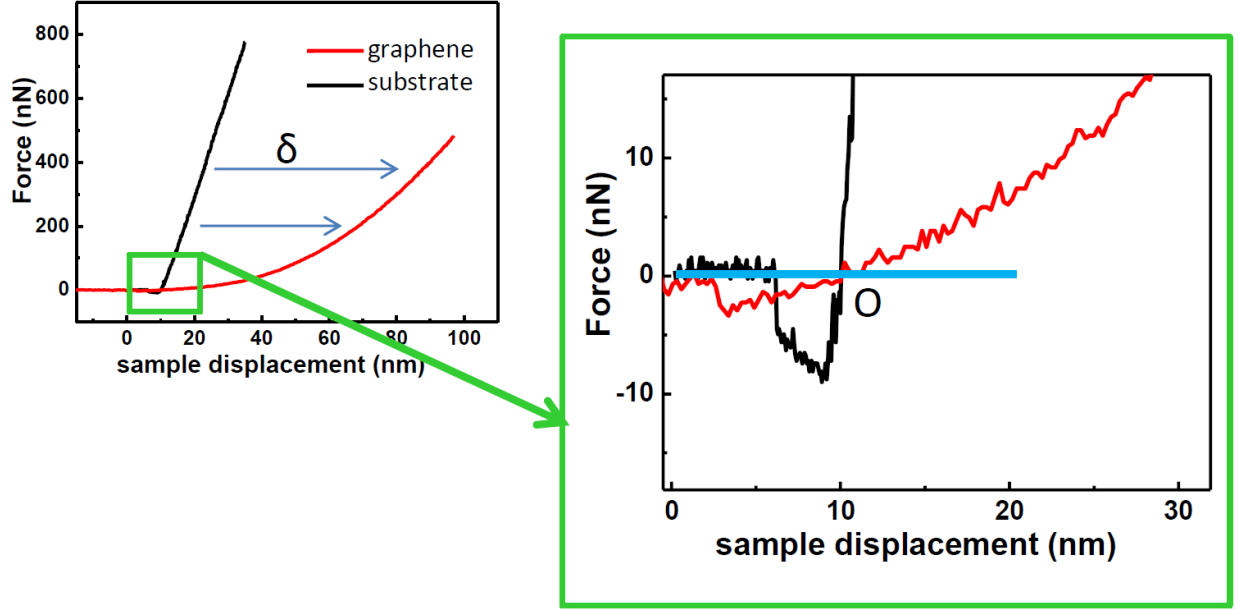


FIG. S1. Representative Force vs. displacement curves acquired on the suspended graphene and  $\text{SiO}_2$  substrate. Zoom in the region of zero force level to highlight the zero displacement point, O.

For an accurate determination of  $\delta$  it is then critical to fix the zero displacement point, and zero force level. This is determined by the point where the curves cross at the zero force level. The experimental noise makes difficult an accurate determination of this level as the data cross several times the horizontal axis. In order to minimize this uncertainty we fitted the curve acquired on the membrane to a third order polynomial and calculated the crossing point of this polynomial with the horizontal axis.  $F(\delta)$  Indentation curves were then fitted to equation 1 in the main text by least square minimization, with  $\sigma_0$  and  $E_{2D}$  as fitting parameters where  $\sigma_0$  corresponds to the stress of the membrane. Figure S2 displays representative Force curves.

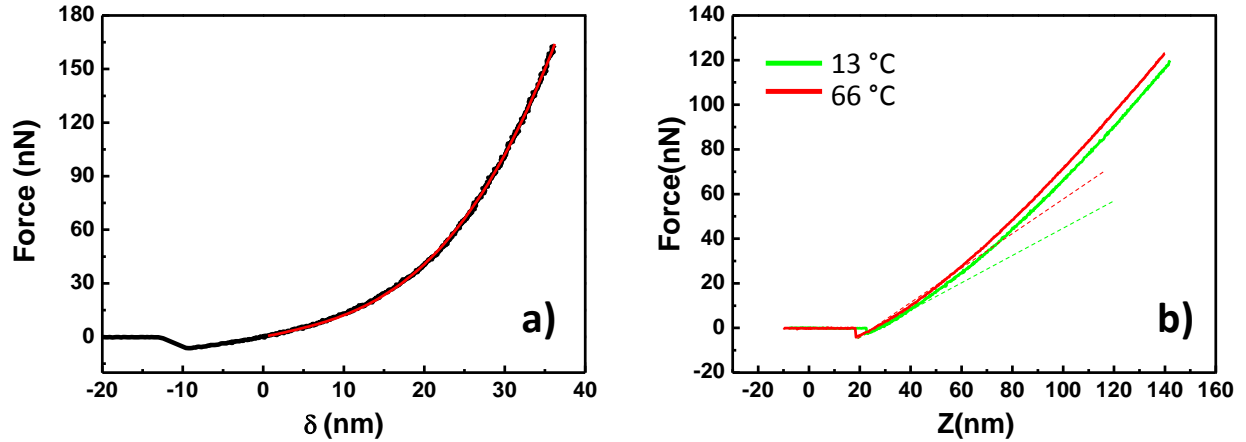


FIG. S2. (a) Force vs. indentation curve measured at the center of the suspended area on a circular drumhead (black). Fitting to eq. 1 in the main manuscript is overlaid in red ( $\sigma_0 = 0.3 \text{ N/m}$ ,  $2a = 750 \text{ nm}$ ,  $E_{2D} = 385 \text{ N/m}$ ). (b) Force vs. sample displacement obtained on a circular graphene drumheads at two different sample temperatures:  $13 \text{ }^\circ\text{C}$  (green), and  $66 \text{ }^\circ\text{C}$  (red). The dashed lines are a guide to the eye to indicate the slope of these curves at low indentations.

### SI3. DEFECT CREATION AND CHARACTERIZATION

**Defect creation:** Irradiation of the samples was performed in a high vacuum (HV) chamber with a base pressure of  $1 \times 10^{-7}$  mbar. The Ar pressure during irradiation was  $5 \times 10^{-5}$  mbar.  $\text{Ar}^+$  energy was set to 140 eV. In our set up the irradiated area fully covers the sample holder, therefore the density of defects can be readily estimated in real time by measuring the ionic current and assuming that each argon ion removes one carbon atom<sup>6,7</sup>.

**Raman spectroscopy:** Raman spectra were performed using a WITEC/ALPHA 300AR Raman confocal microscope at ambient conditions. The laser wavelength and power were 532 nm and 0.7 mW respectively. Graphene monolayers were first identified by optical microscopy and then corroborated by Raman spectroscopy as described in ref. 1.

**Determination of defect density:** Raman spectra of the defected samples present a new peak around  $1350 \text{ cm}^{-1}$ , known as D peak (see Fig. S3). The ratio between the intensities of the D peak and the G peak ( $I_D/I_G$ ) informs about the density of defects induced on the sample.<sup>8</sup> Maps of Raman spectra of the entire graphene flakes were acquired to ensure the homogeneity of the flake. In order to estimate the  $I_D/I_G$  relation we acquire average spectrum always on the same region of the flake.

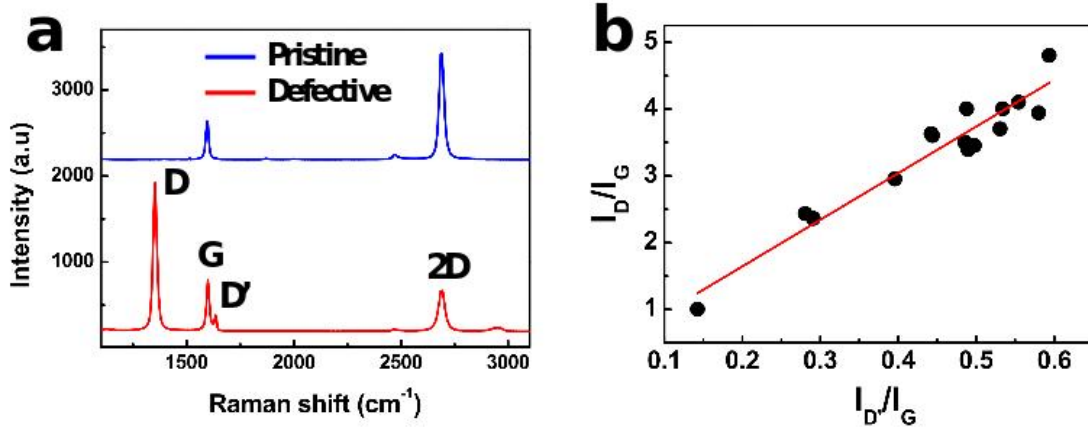


FIG. S3. (a) Raman spectra of a pristine (blue) and a defective graphene membrane (red). Each peak (D, G, D' and 2D) is labeled. (b) Values obtained for  $I_D/I_G$  vs  $I_{D'}/I_G$ , giving  $I_D/I_{D'}=6.9\pm 0.5$ , and, thus, supporting the presence of in-plane vacancies.

The mean distance between defects after each irradiation dose ( $L_D$ ) is estimated according to the expression given in reference<sup>8</sup>, i.e. :

$$\frac{I_D}{I_G} = C_A \frac{(r_A^2 - r_S^2)}{(r_A^2 - 2r_S^2)} \left( e^{-\frac{\pi r_S^2}{L_D}} - e^{-\frac{\pi(r_A^2 - r_S^2)}{L_D}} \right) \quad (1)$$

Where we consider  $r_S=1$  nm,  $r_A=3.1$  nm and  $C_A=A.E_L^{-4}$ , where  $E_L$  is the laser energy and  $A=180$  eV.

**Determination of the nature of defects:** Additional information about the nature of defects can be obtained from the ratio between the intensities of  $D$  and  $D'$  peaks of the Raman spectra as reported in reference<sup>9</sup>. For the case of vacancy-like defects this ratio should be about 7, and about 13 for  $sp^3$  type defects. The slope of the regression line drawn in Fig. S3 yields an average value for this ratio of 6.9, implying the presence of in plane vacancies, instead of  $sp^3$ -type defects (oxidized, hydrogenated, fluorinated, ...). This analysis allows us discarding the presence of chemisorbed molecules on the graphene surface.

**Scanning Tunneling Microscopy (STM) of graphite before and after Ar irradiation:** In order to further corroborate the punctual vacancy nature of defects created by Argon irradiation in the conditions described in the main text, we irradiated HOPG graphite samples in these conditions and imaged them before and after irradiation by STM in air-ambient conditions.

Figure S4 displays STM images of graphite before and after irradiation in the exact

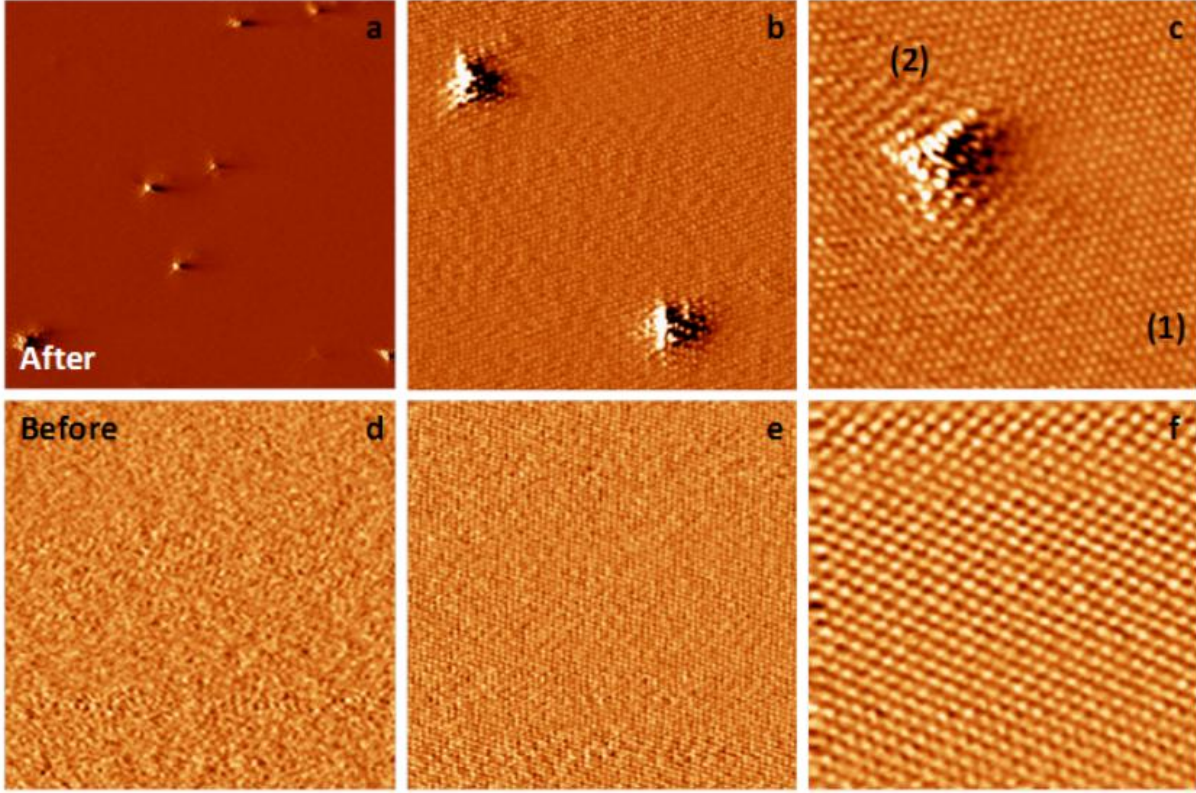


FIG. S4. Atmospheric STM images of graphite before (lower images) and after (upper images) irradiation with Ar ions with the same conditions used for graphene. Image sizes are: panels (a) and (d)  $35 \times 35 \text{ nm}^2$ , panels (b) and (e)  $15 \times 15 \text{ nm}^2$ , panel (c)  $8.5 \times 8.5 \text{ nm}^2$  and panel (f)  $6.3 \times 6.3 \text{ nm}^2$ . Region (2) in panel (c) corresponds to the threefold  $\sqrt{3} \times \sqrt{3}$  perturbation due to the defect, in contrast to the hexagonal atomic periodicity typically observed by STM in pristine graphite (region 1) of the same panel.

same conditions used in the experiments described in the manuscript. While images in graphite prior to irradiation show perfect atomic lattice, atomically resolved images on irradiated samples reveal small defects. These defects, visualized as small protrusions by STM, are uniformly distributed all through the sample. On the regions between defects we always observe a clear and perfect atomic periodicity corresponding to that typically observed by STM in pristine graphite. Our high resolution images of defects (Fig. S4c) are in excellent agreement with those reported previously for single-atom vacancies<sup>7,10,11</sup>. Furthermore, the electronic perturbation near the defects observed as a threefold periodicity surrounding defects identifies them unambiguously as point defects (i.e. smaller than lattice

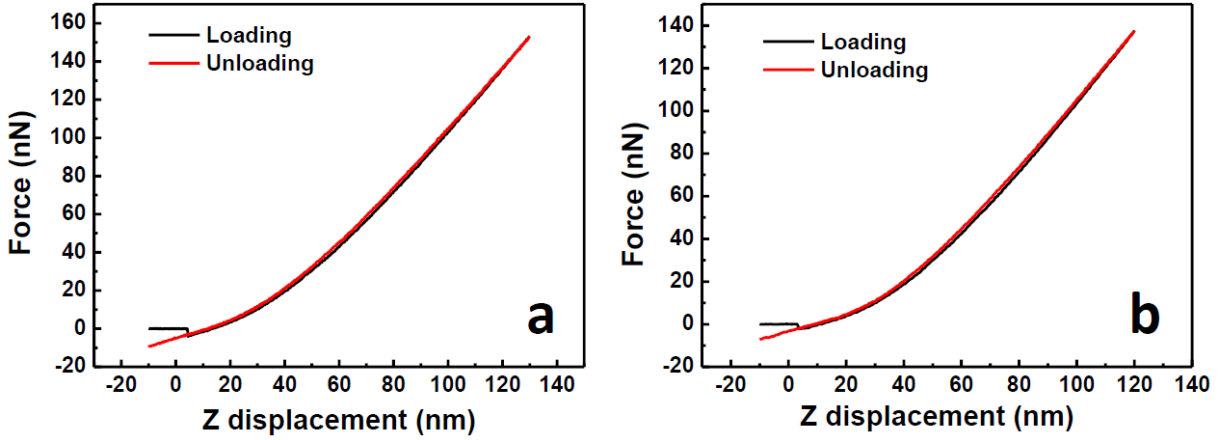


FIG. S5. Loading and unloading Force vs indentation curves acquired on a pristine (a) and a defective (b) graphene drum showing high reproducibility.

spacing). The irradiated graphite surface was scanned in air ambient conditions by STM during 3 consecutive days and we did not observe any trace of image degradation by airborne molecules.

#### SI4. CLAMPING CONDITIONS.

Some authors have reported bad clamping condition and sliding of graphene upon deformation, and suggested that defect creation might improve clamping conditions. We can discard this possibility based on the observation that the stress of the membranes increases faster with temperature in pristine drumheads. If defects improved clamping conditions, prestress of the defective membranes should increase faster. Further support for good clamping and fixed boundary conditions stems for the reproducibility of consecutive  $F(\delta)$  curves, their coincidence in loading and unloading direction (see Fig. S5), and the good fitting to equation 1 in the main text. However, it is worth mentioning that we do observe graphene sliding for temperatures above 80 °C and this effect yields to random measured pretensions with no correlation with temperature. Therefore, we have restricted our measurements to temperatures below 75 °C.

**SI5. CORRELATION BETWEEN THE EVOLUTION OF GRAPHENE TEC AND ELASTIC MODULUS  $E_{2D}$  WITH THE DEFECT CONCENTRATION.**

The here-in presented results support previous studies performed in our group where we observed graphene stiffening upon defect creation<sup>11</sup>. In that work, a similar density of the same type of defects was created in suspended graphene membranes. Characterization of the elastic response of these membranes showed that the elastic modulus of suspended graphene

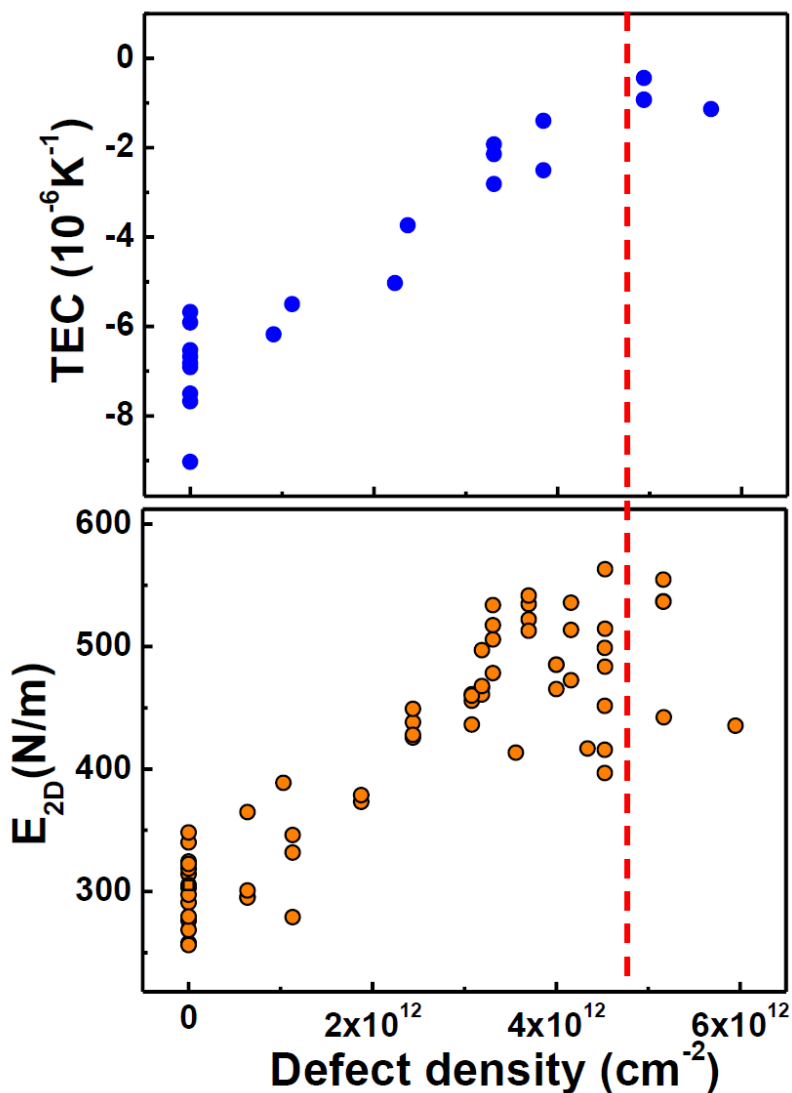


FIG. S6. Experimentally measured TEC (upper panel) and two dimensional elastic modulus (lower panel, reported in ref. 11) as a function of the density of controlled induced mono-vacancies. The red dashed line highlights the defect density at which both magnitudes reach their maximum value.

increases from  $\sim 300$  to  $\sim 550$  N/m for a defect density of 0.2 %. We initially attributed these changes to the suppression of flexural modes in graphene caused by mono-vacancies. Figure S6 shows the data already reported for the elastic modulus of graphene<sup>11</sup> and the here presented data of the TEC of graphene as a function of mono-vacancy density. In the graph, we can appreciate the similarity in the trend of both magnitudes: They increase with defect density until a concentration  $5 \times 10^{12}$  def/cm<sup>2</sup> where they reach their maximum value. This comparison, therefore, supports the notion that graphene elastic response at room temperature is strongly influenced by the presence of out of plane thermal fluctuations.

## Part II: MOLECULAR DYNAMICS SIMULATIONS

### SI6. INTERATOMIC POTENTIALS AND SIMULATION DETAILS.

Molecular dynamics (MD) simulations were performed with the LAMMPS software suite<sup>12</sup> and the reactive force field AIREBO<sup>13,14</sup> to describe the interatomic interactions. AIREBO, the well known second generation of the reactive empirical bond order (REBO) potential, describes a wide range of mechanical<sup>15</sup> and thermal properties<sup>16,17</sup> of pristine<sup>15–17</sup> as well as defective<sup>15,17</sup> graphene. In particular, the torsional term of this force field provides a good description of the low energy out-of-plane phonon modes of graphene ( $ZA, ZO$ ), which are crucial to reproduce the negative TEC of graphene and its change with temperature.

We have modeled a large  $(63a \times 35\sqrt{3}a) \sim 15 \times 15 \text{ nm}^2$  unit cell ( $a$  is the graphene lattice parameter) with different concentrations and distributions of monovacancy defects (see Fig. S12) at different temperatures. The unit cell for the pristine case includes 8820 atoms. We use periodic boundary conditions (PBC) with the corresponding 2D unit cell (for  $x$  and  $y$  directions) and a large vacuum of 40 nm in the  $z$  direction). In all simulations, Newton’s equations of motion have been integrated with the velocity–Verlet integrator with a time step  $\Delta t = 1 \text{ fs}$ . A total simulation time of 40 ns have been used in order to ensure a proper sampling of the thermal fluctuations and to reach the high accuracy on the lattice parameter ( $\sim 10^{-5} \text{ \AA}$ ) needed to determine changes in the TEC (see Fig. S7) and in the stress (see Fig. S10.) For NPT simulations, the temperature and pressure of each simulation are kept constant using the Nose-Hoover thermostat and barostat as implemented in LAMMPS. The PBCs together with the pressure restrain ( $P = 0 \text{ atm}$ ) allow the box size ( $l_x \times l_y$ ) to be relaxed to the equilibrium at each temperature value. For NVT simulations, we use the same protocol but we keep the box size constant (constant volume) using the lattice parameter of pristine graphene at  $T = 210 \text{ K}$ . The lower temperatures (210–300 K) chosen for the theoretical analysis compared to the experiment (283–348 K) help to achieve the precision needed to determine the changes in the lattice parameter with shorter simulation times.

## SI7. SPATIAL AND TIME AVERAGES

### Lattice parameter

The lattice parameters plotted in Figure 3a are determined from the time average (hereafter denoted  $\langle \dots \rangle$ ) of the instantaneous value,  $a(t)$ , for each time step over the last 20 ns, [ $t_i = 20$  ns ,  $t_f = 40$  ns], of the corresponding NPT simulation:

$$\langle a(t) \rangle = \frac{1}{\sqrt{N_f}} \sum_{t_i}^{t_f} a(t); \quad a(t) = \sqrt{\frac{l_x \cdot l_y}{63 \cdot 35 \sqrt{3}}}. \quad (2)$$

where  $a(t)$  is determined from the instantaneous dimensions  $l_x(t)$  and  $l_y(t)$  of the unit cell.  $N_f = (t_f - t_i)/\Delta t$  is the number of time steps that are included in the average. For details on the convergence of  $\langle a(t) \rangle$  (see Fig. S7).

### Spatially averaged out-of-plane fluctuation $h(t)$

We have evaluated for each time step,  $t$ , the spatial average,  $z(t)$ , and standard deviation (RMS),  $h(t)$ , of the  $z$  coordinate of the  $N$  atoms of the membrane:

$$h(t) = \frac{1}{\sqrt{N}} \left[ \sum_{i=1}^N (z_i(t) - z(t))^2 \right]^{1/2}; \quad z(t) = \frac{1}{N} \sum_{i=1}^N z_i(t) \quad (3)$$

$h(t)$  represents the amplitude of the out-of-plane fluctuations of the membrane.

### Time-averaged out-of-plane fluctuation per atom (2D maps) $\langle h(\bar{r}_i) \rangle$

The 2D maps in Figure 4b display  $\langle h(\bar{r}_i) \rangle = \langle (z_i(t) - z_i)^2 \rangle^{1/2}$ , with  $z_i(t)$  the instantaneous  $z$  coordinate for atom  $i$  in the unit cell, and  $z_i = \langle z_i(t) \rangle$ , its time average.

### Time-averaged Thermal stress and per-atom stress tensor

The thermal stress  $\sigma$  is linked with the per-atom-stress tensor<sup>16</sup>:

$$\sigma = \frac{1}{A} \sum_{i=1}^N (K_{xx}^i + K_{yy}^i + K_{zz}^i) = \frac{1}{N} \sum_{i=1}^N \frac{1}{A_{at}} (K_{xx}^i + K_{yy}^i + K_{zz}^i), \quad (4)$$

where  $K_{aa}^i = K_{aa}(\bar{r}_i)$  are the diagonal components ( $a = x, y, z$ ) of the per-atom stress tensor for atom  $i$ ;  $A = NA_{at}$  is the total area of the unit cell, with  $A_{at}$  the area per atom, and  $N$  the number of atoms.

We have calculated  $\sigma$  in our NVT simulations as a time average over the last 20 ns of the instantaneous pressure  $P(t)$ , using the relations:

$$\sigma = -\frac{3V}{A} \langle P(t) \rangle; \quad P(t) = -\frac{1}{3V} \sum_{i=1}^N [K_{xx}^i(t) + K_{yy}^i(t) + K_{zz}^i(t)]. \quad (5)$$

For details on the convergence of  $\langle\sigma\rangle$  see Fig. S10.

The 2D stress maps shown in Figure 5b in the main text correspond to the time average (last 20 ns) of the in-plane stress per atom (normalized by  $A_{at}$ )  $\langle K_{\parallel}(\bar{r}_i)\rangle$ :

$$\langle K_{\parallel}(\bar{r}_i)\rangle = \frac{1}{2A_{at}}\langle K_{xx}(\bar{r}_i, t) + K_{yy}(\bar{r}_i, t)\rangle \quad (6)$$

Our simulations confirmed that the contribution of the out-of-plane stress  $\langle K_{zz}(\bar{r}_i)\rangle$  is approximately 10 times smaller than the in-plane contribution.

## S18. CONVERGENCE OF THE TIME AVERAGES AND DEPENDENCE ON DEFECT CONCENTRATION AND TEMPERATURE

Here we present further information on the convergence of the time averages for the lattice parameter in NPT simulations and the stress in NVT simulations, the TEC dependence on the defect distribution and the number of sampling temperatures, and the thermal stress as a function of temperature for different defect concentrations.

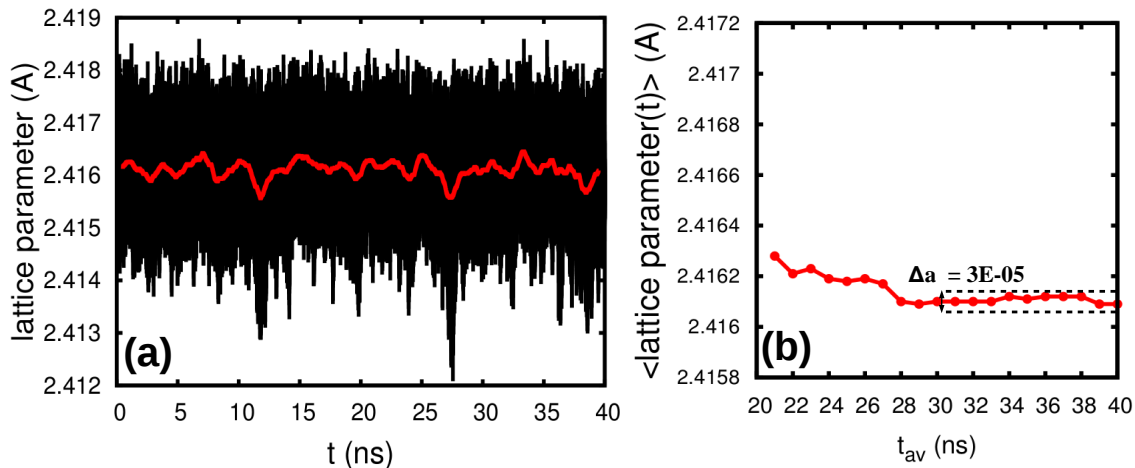
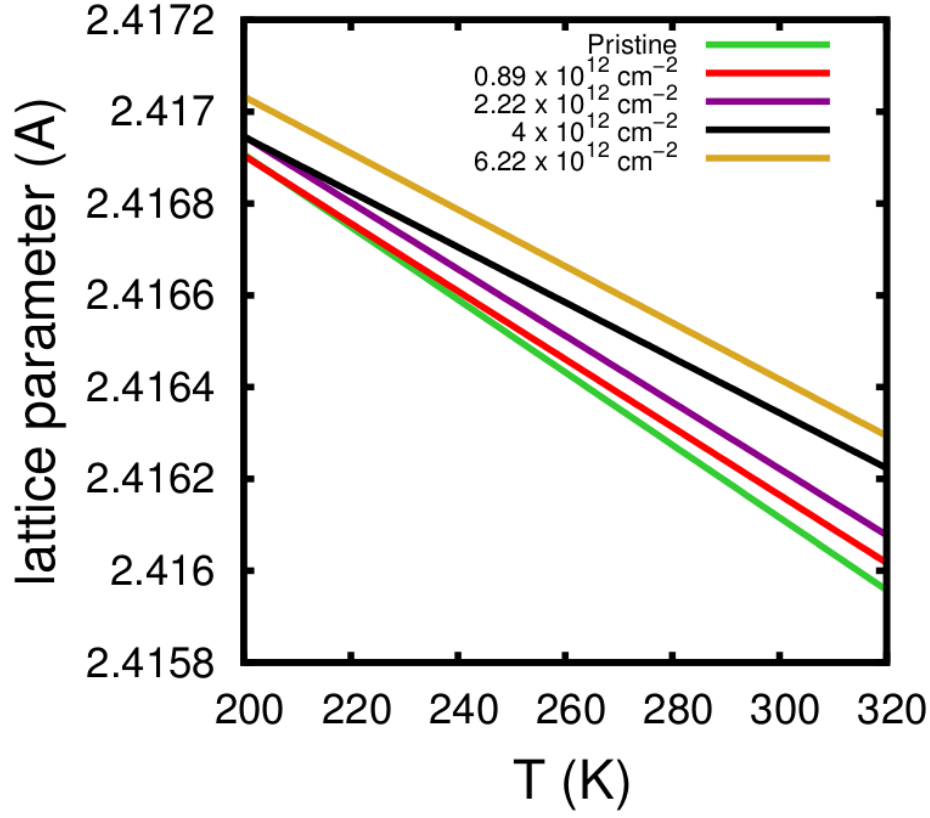


FIG. S7. **Determination of the equilibrium lattice parameter from NPT simulations**

(a) Instantaneous value  $a(t)$  of the lattice parameter (black) and running average (including the previous  $10^6$  time steps, red) for the pristine monolayer at 300 K. (b) Incremental time average (red dots)  $\langle a \rangle(t_{av}) = \frac{1}{\sqrt{N_f}} \sum_{t_i}^{t_{av}} a(t)$ , with  $N_f = (t_{av} - t_i)/\Delta t$ , calculated for the last 20 ns of the simulation shown in (a),  $t_i = 20$  ns,  $t_{av} = 21, \dots, 40$  ns. The red line is a guide to the eye. These results confirm that the simulations are long enough to achieve a precision ( $\sim 10^{-5}$  Å) in the determination of the lattice parameter. The ordinate scale is identical to Fig. 3a in the main manuscript. The lattice parameter values plotted in Fig. 3a in the main manuscript and used for the TEC calculation are the mean value of the last ten values of  $\langle a \rangle(t_{av})$ ,  $t_{av} = 31, \dots, 40$  ns for each NPT simulation.



Defect density ( $10^{12} \text{ cm}^{-2}$ )	0	0.89	2.22	4 (i conf.)	4 (ii conf.)	4 (iii conf.)	4 (iv conf.)	6.22
$a_{T=210K}$ (Å)	2.41686	2.41684	2.41684	2.41695	2.41686	2.41690	2.41696	2.41699
$a_{T=240K}$ (Å)	2.41653	2.41662	2.41668	2.41663	2.41670	2.41666	2.41662	2.41676
$a_{T=270K}$ (Å)	2.41640	2.41632	2.41651	2.41649	2.41645	2.41651	2.41653	2.41660
$a_{T=300K}$ (Å)	2.41611	2.41620	2.41617	2.41639	2.41630	2.41631	2.41633	2.41643
$\mathbf{m}$ ( $10^{-6} \text{ ÅK}^{-1}$ )	-7.91342	-7.39712	-7.24532	-6.02112	-6.45572	-6.4118	-6.61172	-6.16047
$a_0$ (Å)	2.41922	2.41923	2.41936	2.41938	2.41938	2.41938	2.41938	2.41995
<b>TEC</b> ( $10^{-6} \text{ K}^{-1}$ )	-3.27106	-3.05763	-2.99473	-2.4887	-2.66834	-2.65018	-2.73282	-2.5457

FIG. S8. Lattice parameter as a function of temperature for different defect densities.

(top) Linear fits for  $a_T$  for each defect concentration. The fit for  $C_{def} = 4 \times 10^{12} \text{ cm}^{-2}$  corresponds to the (i) configuration (See Figure S12). (bottom) Lattice parameter  $a_T$  for each temperature and defect concentration, slope of the fits ( $\mathbf{m}$ ) plotted above, lattice parameter value at  $T = 0 \text{ K}$  ( $a_0$ ), and calculated **TEC**.

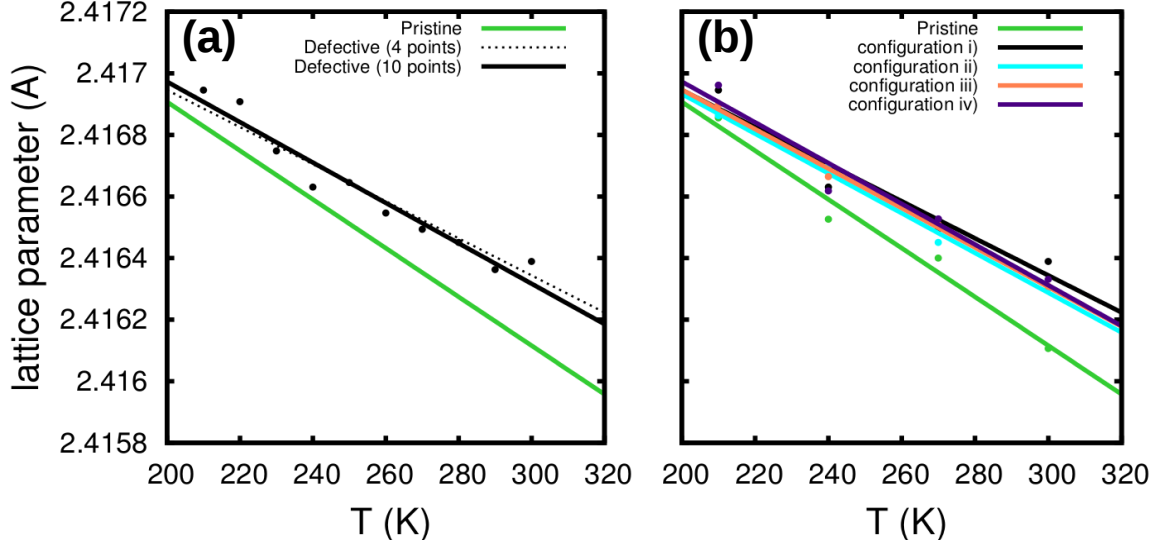


FIG. S9. **TEC dependence on the number of sampling temperatures and defect distribution.** (a) Lattice parameter versus  $T$  for one of the defective cases ( $C_{def} = 4 \times 10^{12} \text{ cm}^{-2}$ , configuration (i)) and the corresponding fit using 10 different temperatures (solid black line). The fits for the pristine case (solid green line), and the same defect configuration (dotted black line) using 4 different temperatures plotted in Fig. 3a in the main manuscript are shown for comparison. No significant changes in the TEC are found when using a denser sampling of the same temperature range, supporting our choice of sampling only four temperatures for the rest of the TEC calculations. (b) Lattice parameter versus  $T$  for the four different defect configurations studied for  $C_{def} = 4 \times 10^{12} \text{ cm}^{-2}$  (see Fig. S12). The lines are the corresponding linear fits. The results for the pristine case (green) are shown for comparison. These results rule out a strong dependence of the TEC with the defect distribution for a given defect concentration.

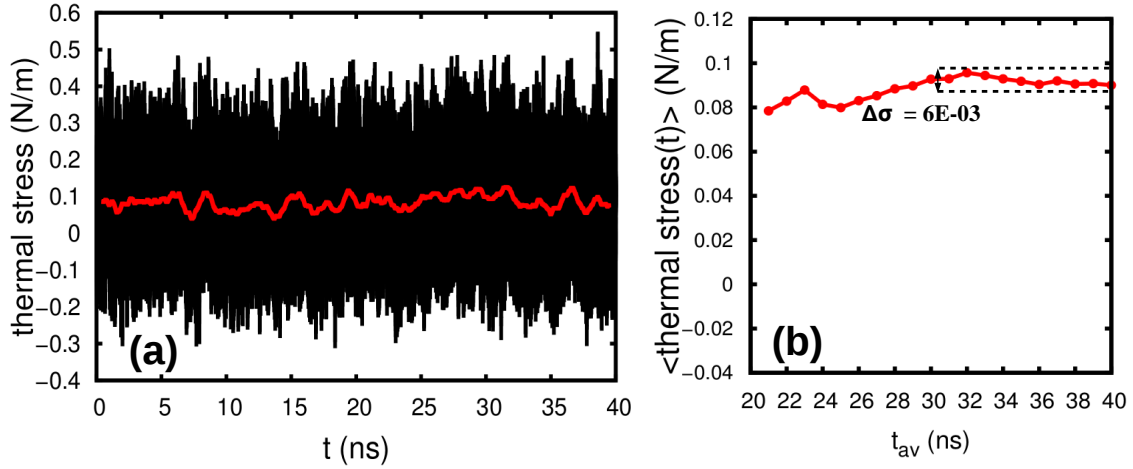


FIG. S10. **Determination of the thermal stress from NVT simulations.** The procedure followed to compute the thermal stress and determine its convergence follows closely the one used for the lattice parameter (see Fig. S7). **(a)** Instantaneous value of the thermal stress (pristine monolayer, 300 K) (black) and running average (including the previous  $10^6$  time steps, red). **(b)** Incremental time average (red dots)  $\langle \sigma \rangle(t_{av})$  for the last 20 ns of the simulation. The ordinate scale is identical to Fig. 5a in the main manuscript. The thermal stress values plotted in Fig. 5a in the main manuscript are the mean value of the last ten values of  $\langle \sigma \rangle(t_{av})$ ,  $t_{av} = 31, \dots, 40$  ns for each NVT simulation.

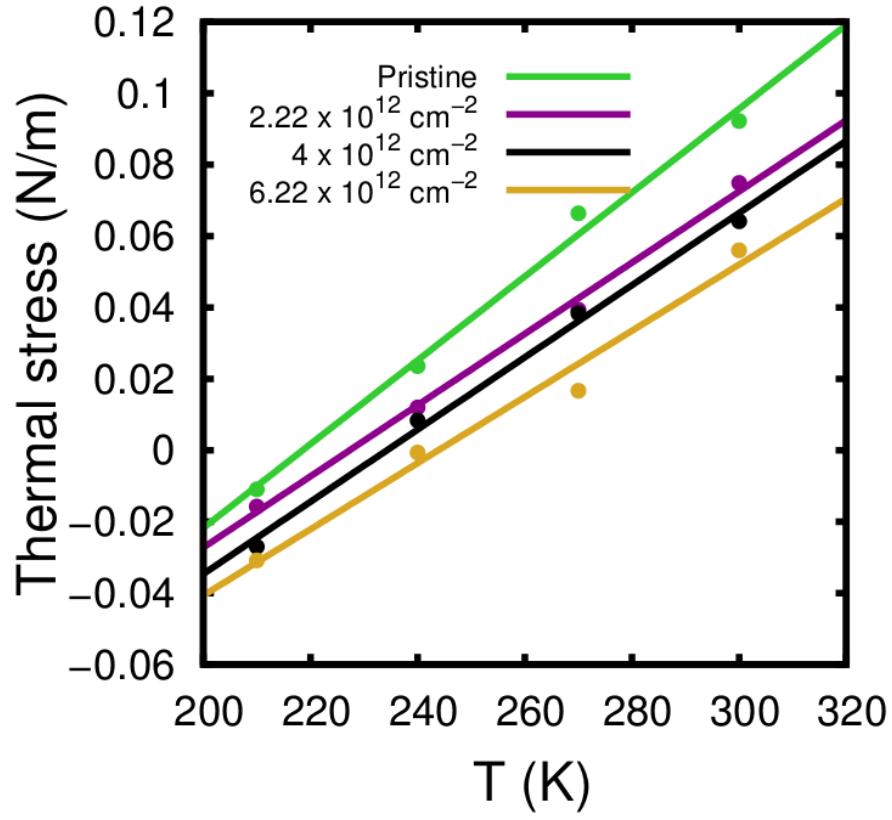


FIG. S11. **Thermal stress as a function of temperature for different defect concentrations.** Thermal stress versus  $T$  for each defect concentration (bullets) and the corresponding linear fits (lines) The result for  $C_{def} = 4 \times 10^{12} \text{ cm}^{-2}$  corresponds to defect configuration (i) in Fig. S12.

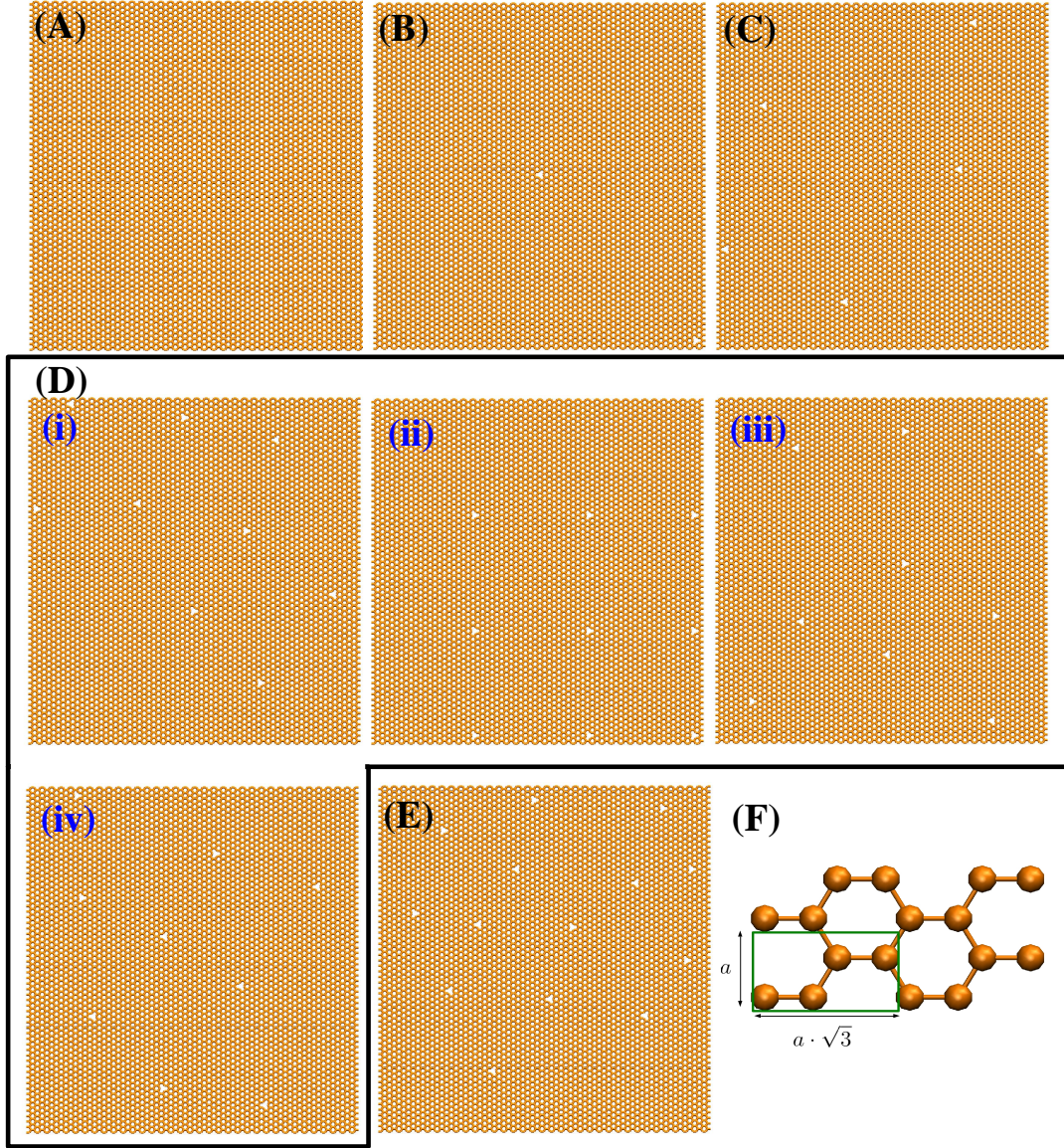


FIG. S12. **Atomic configurations for the defects densities considered in this work.** (A)  $15 \times 15 \text{ nm}^2$  pristine sheet unit cell –corresponding to  $63 \times 35$  the  $a \times a\sqrt{3}$  unit cell (green rectangle) shown in (F)– with 8820 carbon atoms. (B)-(E) Defective sheets, built by removing carbon atoms from the pristine membrane, and characterized by the defect concentration ( $C_{def}$ ) and the average defect-defect distance ( $d_{def}$ ): (B)  $C_{def} = 0.89 \times 10^{12} \text{ cm}^{-2}$ ;  $d_{def} = 10.6 \text{ nm}$ ; (C)  $C_{def} = 2.22 \times 10^{12} \text{ cm}^{-2}$ ;  $d_{def} = 6.70 \text{ nm}$ ; (D)  $C_{def} = 4 \times 10^{12} \text{ cm}^{-2}$ ;  $d_{def} = 5 \text{ nm}$ ; (E)  $C_{def} = 6.22 \times 10^{12} \text{ cm}^{-2}$ ;  $d_{def} = 4.06 \text{ nm}$ . For the (D) case, the four different defect distributions, (i) to (iv), analyzed for this concentration of defects are shown. The results shown in the main manuscript for (D) have been obtained using configuration (i).

- 
- <sup>1</sup> A. C. Ferrari, J. C. Meyer, V. Scardaci, C. Casiraghi, M. Lazzeri, F. Mauri, S. Piscanec, D. Jiang, K. S. Novoselov, S. Roth, and A. K. Geim, *Phys. Rev. Lett.* **97**, 187401 (2006).
- <sup>2</sup> C. Lee, X. Wei, J. W. Kysar, and J. Hone, *Science* **321**, 385 (2008).
- <sup>3</sup> I. Horcas, R. Fernandez, J. M. Gomez-Rodriguez, J. Colchero, J. Gomez-Herrero, and A. M. Baro, *Rev. Sci. Instrum.* **78**, 013705 (2007).
- <sup>4</sup> M. R. Begley and T. J. Mackin, *J. Mech. Phys. Solids* **52**, 2005 (2004).
- <sup>5</sup> J. E. Sader, J. W. M. Chon, and P. Mulvaney, *Rev. Sci. Instrum.* **70**, 3967 (1999).
- <sup>6</sup> O. Lehtinen, J. Kotakoski, A. V. Krashenninnikov, A. Tolvanen, K. Nordlund, and J. Keinonen, *Phys. Rev. B* **81**, 153401 (2010).
- <sup>7</sup> M. M. Ugeda, I. Brihuega, F. Guinea, and J. M. Gómez-Rodríguez, *Phys. Rev. Lett.* **104**, 096804 (2010).
- <sup>8</sup> L. G. Cançado, A. Jorio, E. H. M. Ferreira, F. Stavale, C. A. Achete, R. B. Capaz, M. V. O. Moutinho, A. Lombardo, T. S. Kulmala, and A. C. Ferrari, *Nano Lett.* **11**, 3190 (2011).
- <sup>9</sup> A. Eckmann, A. Felten, A. Mishchenko, L. Britnell, R. Krupke, K. S. Novoselov, and C. Casiraghi, *Nano Lett.* **12**, 3925 (2012).
- <sup>10</sup> H. A. Mizes and J. S. Foster, *Science* **244**, 559 (1989).
- <sup>11</sup> G. López-Polín, C. Gómez-Navarro, V. Parente, F. Guinea, M. Katsnelson, F. Pérez-Murano, and J. Gómez-Herrero, *Nat. Phys.* **11**, 26 (2014).
- <sup>12</sup> S. Plimpton, *J. Comput. Phys.* **117**, 1 (1995).
- <sup>13</sup> S. J. Stuart, A. B. Tutein, and J. A. Harrison, *J. Chem. Phys.* **112**, 6472 (2000).
- <sup>14</sup> D. W. Brenner, O. A. Shenderova, J. A. Harrison, S. J. Stuart, B. Ni, and S. B. Sinnott, *J. Phys. Condens. Matter* **14**, 783 (2002).
- <sup>15</sup> D. Kvashnin and P. Sorokin, *J. Phys. Chem. Lett.* **6**, 2384 (2015).
- <sup>16</sup> W. Gao and R. Huang, *J. Mech. Phys. Solids* **66**, 42 (2014).
- <sup>17</sup> N. C. B. Mostério and A. F. Fonseca, *Phys. Rev. B* **89**, 195437 (2014).